Nano Energy 41 (2017) 573–582

Contents lists available at ScienceDirect

Nano Energy

journal homepage: www.elsevier.com/locate/nanoen

Full paper

# Designing solid-electrolyte interphases for lithium sulfur electrodes using ionic shields

Mun Sek Kim[a], Min-Seop Kim[b], Vandung Do[c], Young Rok Lim[d], In Wook Nah[a], Lynden A. Archer[e,*], Won Il Cho[a,*]

[a] Center for Energy Convergence Research, Korea Institute of Science and Technology, Hwarangno 14-gil 5, Seongbuk-gu, Seoul 02792, Republic of Korea
[b] Department of Materials Science and Engineering, Korea University, 145 Anam-ro, Seongbuk-gu, Seoul 02841, Republic of Korea
[c] Department of Energy and Environment Technology, Korea University of Science and Technology, Gajeong-ro 217, Yuseong-gu, Daejeon 34113, Republic of Korea
[d] Department of Chemistry, Korea University, Sejong-ro 2511, Sejong 30019, Republic of Korea
[e] Department of Chemical and Biomolecular Engineering, Cornell University, Ithaca, NY 14853-5201, USA

ARTICLE INFO

*Keywords:*
Lithium metal anodes
Ionic shields
Charged nanoparticles
Artificial solid-electrolyte interphases
Lithium sulfur batteries

ABSTRACT

Lithium metal is among the most sought-after anode chemistries for next-generation electrical energy storage due to its high theoretical capacity (3860 mAh $g^{-1}$) and low reduction potential (− 3.04 V *vs* S.H.E.). To realize its promise, reactive Li anodes must be paired with high-energy conversion cathodes, such as sulfur or oxygen. Chemical and physical instability at both electrodes pose formidable challenges to development of practical lithium metal batteries. These instabilities are compounded by problems with active material loss and anode passivation when Li is paired with conversion cathodes, such as elemental sulfur. Here, we report on design principles and a process for creating artificial solid electrolyte interphases composed of ionic shields that are able to stabilize electrochemical processes at both the anode and cathode of Li-S electrochemical cells. We show that ASEI composed of negatively-charged nanoparticles on Li stabilize deposition of Li at the anode by multiple fundamental mechanisms. A similar concept is used to design interphases composed of positively charged conductive nanoparticles at the cathode and shown to be effective at intercepting dissolved polysulfide anions and for enhancing sulfur reutilization. We combine the two ASEI design strategies to create Li-S cells based on high-loading sulfur cathodes and demonstrate their long-term cycling stability.

## 1. Introduction

As consumer demand for portable electrical devices escalate with the rise of the microelectronics industry, expeditious advancement of commercializable electrical energy storage (EES) systems is regarded as a requirement. An EES system that offered substantial improvements in energy and power densities with high electrochemical reversibility is therefore a highly sought after goal. In order to realize this goal, lithium metal batteries (LiMBs) were first proposed in the 1970s, but deployment of these cells was impeded by their poor Coulombic efficiency and cyclability, as well as by the tendency of lithium to form rough deposits upon battery recharge that led to the proliferation of dendrites and other morphological instabilities (*e.g.* orphaned Li) that reduce battery lifetime and trigger safety issues. Lithium ion batteries (LiBs) with ion intercalation based electrodes overcome many of these problems and were first commercialized in 1991. Notwithstanding the commercial success of LiBs, new types of rechargeable batteries based on metallic anodes, such as Li-metal [1–4]/sulfur [5–9]/air [10–12], Na-metal [13–15]/sulfur [16,17]/air [18,19], and Al-metal [20,21]/sulfur [22,23]/air [24–26], continue to garner significant attention by researchers because they offer high energy density and prospective economic benefits [27,28].

Among these cell chemistries, Lithium-sulfur batteries (Li-SBs) are arguably the most promising candidates to supplant conventional LiBs as the rechargeable battery platform of choice, both because of the high theoretical specific capacities of the Li anode (3860 mAh $g^{-1}$) and sulfur cathode (1675 mAh $g^{-1}$) and the low cost and high earth abundance of the active cathode materials [29]. Such cells are however not commercially viable today because parasitic physical and electrochemical processes at both electrodes deplete the active species and limit lifetime [28]. An extensive body of work is now available that describes the physico-chemical processes responsible for these modes of cell failure. Three specific problems have been diagnosed that provide the foundation for the current study: i) lithium polysulfide (LiPS) dissolution and shuttling; [30,31] ii) electrode passivation by reaction with and redeposition of dissolved active species, [3,32–41] and iii)

* Corresponding authors.
*E-mail addresses:* laa25@cornell.edu (L.A. Archer), wonic@kist.re.kr (W.I. Cho).

http://dx.doi.org/10.1016/j.nanoen.2017.10.018
Received 11 August 2017; Received in revised form 30 September 2017; Accepted 6 October 2017
Available online 07 October 2017

proliferation breakage and short-circuits induced by lithium dendrites [3,4,33,35,38–40,42–45]. $LiNO_3$ and LiPS have emerged as powerful electrolyte additives in ether-based solvents for stabilizing lithium anodes [39]. Unfortunately, continuous dissolution of LiPS and consumption of $LiNO_3$ during repeated cell cycles dissipate the beneficial effects of these additives when cells are subjected to practical performance cycles, including repeated deep discharges and high active material loadings in the cathode to produce the $> 350\ W\ h\ kg^{-1}$ cell-level specific energy promised by Li-SBs [46]. As lithium metal anode improvement is essential for practical application of Li-SBs, [47] several anode protection techniques are reported accordingly. Kozen et al. proposed an atomic layer deposition method to protect Li with ~ 14 nm thick $Al_2O_3$ thin film from side reactions with electrolyte and active materials; however, relatively high interfacial impedance and limited lithium migration reversibility are reported [38]. Ma et al. proposed *in-situ* formation of ionically conducting $Li_3N$ protective layer on lithium anode that helps $Li^+$ migration for Li-SBs [48]. Although formation of the ion selective protection layer is noteworthy, small cracks formed on the protective layer under volume changes of the anode can quickly proliferate lithium dendrites which destabilizes lithium migration and side reactions as the protective layer is thin (200–300 nm) and non-porous. Furthermore, hybrid anode structure is developed to protect lithium metal anode and alleviate undesired side reactions for Li-S system [49]. Providing lithium host such as graphite on top of lithium metal is beneficial for controlling side reactions and lithium preservation, but the dual configuration anode reduces the energy density for practical Li-SBs. Therefore, advanced lithium protection layer should have high conductivity with ion selectivity, high physico-chemical stability, and semi-hosting features for lithium, which we aim to develop in this study.

Herein, we consider the role of artificial solid electrolyte interphase (ASEI) layers composed of ionic shields deployed on both anode and cathode facing a separator (Fig. 1) in remedying the problems of Li-SBs. We focus in particular on cell designs that do not utilize $LiNO_3$ electrolyte additives to determine the design rules for ionic shields that are able to address current limitations of Li-SBs. To fabricate the ASEI used in the study, lithium terminated sulfonated titania (LTST) nanoparticles are synthesized *via* one-pot solution method as an ingredient for the Li protection film. Then, the film is created on a solid substrate *via* Langmuir-Blodgett scooping (LBS) method [8,9] to be directly transferred to Li using a roll-press machine to fabricate LTST coated Li (LTST-Li). These processes are briefly summarized in Fig. 1a. Functionalized metal-oxide nanoparticles on Li are thought to serve two functions: i) to maintain high conductivity at the anode/electrolyte interface when the cell is polarized and ii) to electrostatically shield the Li anode and to prevent interfacial accumulation of soluble anionic polysulfide components at the anode [50]. To ensure good ionic conductivity and preservation of the protection layer over repeated volumetric changes of the Li anode, the nanoporous hybrid electrolyte composed of LTST nanoparticles is directly deposited by *ex-situ* method on Li to form a robust conformal coating. On the Li electrode, the functionalized metal-oxide nanoparticles spontaneously form a porous framework that stabilizes the anode by a combination of mechanical [3] and dimensional effects [4]. The ASEI on the cathode side was created using Air-brush technique with ethanol as suspending medium to deposit, on the cathode facing side of the separator, a thin coating of hybrid nanostructures composed of polyethylenimine attached reduced graphene oxide (PEIrGO). The coating is designed to simultaneously enable localization of solvated polysulfide (PS) anions (*via* electrostatic attraction of $PS^-$ to the multi-amine groups in PEI) and to enable re-utilization of the captured material (*via* facilitated electron transport in rGO). The PEIrGO synthesis and procedure used for creating the PEIrGO ASEI on the separator are summarized in Fig. 1b. The overall, cell design illustrating both ASEIs is summarized in Fig. 1c. We show later that the combination of high sulfur utilization and protection of the Li anode lead to cells with prolonged electrochemical and cycling stability.

## 2. Material and methods

### 2.1. Materials synthesis

#### 2.1.1. Lithium terminated sulfonated $TiO_2$ (LTST) nanoparticle

3 g of $TiO_2$ nanoparticles (~ 30 to 50 nm, 99% purity, Rutile, Inframat Advanced Materials™) are mixed with 125 ml deionized (DI) water and sonicated for 30 min at room temperature. 3 ml of 3-(trihydroxysilyl)-1-propanesulfonic acid (30–35% in water, Gelest) is added

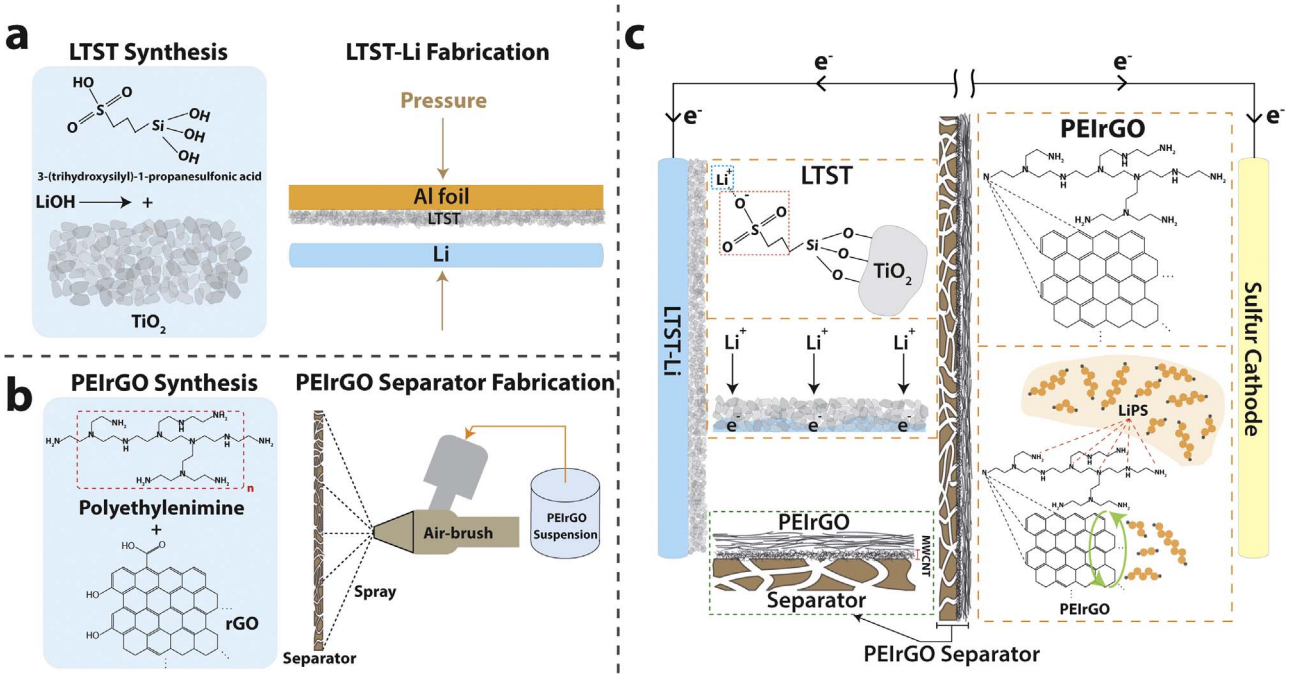


**Fig. 1.** Schematic illustration showing ASEI designs for Li-SB electrodes, and their respective fabrication processes. **a)** LTST synthesis (left) and LTST-Li fabrication process (right). **b)** PEIrGO synthesis (left) and PEIrGO separator fabrication (right) processes. **c)** Illustration of synergistic effects of LTST and PEIrGO ASEIs for Li-SBs.

dropwise to the dispersed suspension and stirred overnight at room temperature to attach the silane groups. Then, the suspension is sonicated again for 30 min and restirred for 30 min at room temperature before neutralization step. Then concentrated LiOH is slowly added to the reactants until pH of 7, and the reactants are stirred for 3 h at room temperature to terminate $Li^+$. After the full reaction, the LTST nanoparticles are centrifuged 10 times with DI water to remove the excess silanes. The cleaned LTST nanoparticles are dried in a convection oven at 60 °C for overnight. Note that the $TiO_2$ nanoparticles are not well dispersed in DI water at first, but well dispersed suspension is obtained during and after the silane attachments. The functionalization effect, therefore, can be seen by observing dispersion of LTST nanoparticles in water (Fig. S1).

#### 2.1.2. Polyethylenimine attached reduced graphene oxide (PEIrGO)

The PEIrGO is synthesized in three steps: 1) synthesizing graphene oxide *via* modified Hummer's method, [51,52] 2) reducing graphene oxide using hydrogen gas at high temperature, 3) attaching PEI on the reduced graphene oxide. Briefly for graphene oxide synthesis, graphite flakes (Sigma Aldrich) are dispersed in concentrated sulfuric acid (Sigma Aldrich) and cooled to 0 °C. The potassium permanganate (Sigma Aldrich) solution is then added dropwise at temperature below 10 °C. After, distilled water and hydrogen peroxide is added to the solution. The graphene oxides are then collected by filtrating the suspension with DI water. The synthesized graphene oxides are reduced under ambient pressure with hydrogen gas (100 sccm at 800 °C for 150 min). The reduced graphene oxides are then dispersed in water for PEI attachment process. 300 mg of reduced graphene oxides are dispersed in water (500 ml) followed by 1 h of sonication. Then, 500 mg of branched PEI (Sigma Aldrich, avg Mw ~ 25,000 by LS and avg Mn ~ 10,000 by GPC, branched) is added to the reduced graphene oxide dispersed solution and sonicated for 1 h. The solution is then placed into an oil bath and stirred at 95 °C for 24 h. The PEIrGO is then cleaned by centrifuging the reacted suspension for 10 times each with DI water. The cleaned PEIrGO particles are stored as suspension with DI water. The concentration of PEIrGO in the suspension is 10 mg PEIrGO per 1 ml DI water. The synthesized PEIrGO exhibits about 9% nitrogen content *via* X-ray photoelectron spectroscopy (XPS) analysis.

### 2.2. Artificial solid electrolyte interphase (ASEI) film preparation

#### 2.2.1. LTST ASEI film fabrication

0.5 g of the synthesized LTST nanoparticles are dispersed in 20 ml of pure ethanol and sonicated for 30 min to make LTST suspension. 3 μm thick LTST ASEI is created on Al foil *via* Langmuir-Blodgett scooping (LBS) method.[8,9] Briefly, Al foil is cut to 4.5 cm × 8 cm. Then, the foil is submerged to water filled beaker, and the LTST suspension is constantly injected at water surface to form LTST film. By simultaneously raising the submerged foil, LTST film is continuously deposited. Finally, the LTST coated Al foil is dried on a hot plate at 110 °C to remove remaining water. Note that LTST ASEI consists multilayers of LTST nanoparticles as multilayer LB deposition is allowed for LBS process. Similarly, other substrates such as Cu foil, $Si/SiO_2$, and glass slide are used to coat LTST *via* LBS method to prepare samples for other characterizations and measurements. The areal mass loading of coated LTST nanoparticle is ~ 380 μg $cm^{-2}$.

#### 2.2.2. LTST coated Li (LTST-Li) fabrication

The LTST ASEI film is transferred onto lithium *via* roll-press technique. Under dry atmospheric condition, lithium is sandwiched with ASEI coated Al foil and Cu mesh, and the sandwiched lithium is covered with Mylar films. Then the stacked films are uniformly pressed *via* roll-press machine with the cylinder distance of 0.15 mm and rolling rate of 1 cm $s^{-1}$. After the press, Mylar films are removed, and Al foil is peeled-off from the lithium. The coated lithium is cut into circular disk (diameter of 1.5 cm) for the coin cell measurements.

#### 2.2.3. PEIrGO ASEI coated separator

Thin layer (1 μm thick) of multi-walled carbon nanotube (Sigma Aldrich, > 98% carbon basis, O.D. × L 6–13 nm × 2.5–20 μm) is coated onto a separator (Celgard 2500) as an adhesion layer for PEIrGO *via* Air-spray method. After the pre-coating, the PEIrGO (~ 10 μm thick) is then coated on top of the MWCNT/separator *via* Air-spray method. The PEIrGO dispersion in ethanol (~ 2 mg $ml^{-1}$) is used for Air-spray ink. During the air spraying, the separator is placed onto a hotplate at 80 °C to accelerate solvent evaporation. The PEIrGO coated separator is then dried in convection oven for one day at 60 °C. The dried separator is then punched into circular disk (1.8 cm diameter) for coin cell measurements. The areal mass loading of coated materials is ~ 300 μg $cm^{-2}$. The mechanical stability of the PEIrGO separator is shown in Fig. S2.

### 2.3. Electrochemical measurements

For sulfur carbon (S/C) composite, sulfur powder (Sigma, 99.98%) is well mixed with multi-walled carbon nanotube (MWCNT) with a weight ratio of 8:2. The mixed S/MWCNT composite is heated to 155 °C for 8 h to obtain S/C composite. The obtained S/C composite shows 79% of sulfur content (Fig. S3). The sulfur electrode is prepared by casting a slurry that contains 80% of S/C composite, 5% of Super P carbon, 5% of rGO, 10% of aqueous binders (polyvinylpyrrolidone 5%, polyethylene oxide 4%, sodium carboxymethyl cellulose 1%). The casted sulfur cathode is dried at 60 °C for overnight. The fabricated sulfur cathode has pure sulfur loading and content of 3 mg $cm^{-2}$ and 64% with a total electrode mass of 4.7 mg $cm^{-2}$. The sulfur content after including the separator coating materials is 60%. The prepared sulfur cathode is then punched into circular disk (1.3 cm diameter) for Li-S coin cell measurements.

Two electrolyte systems are used in this work: i) 1 M Bis(trifluoromethane)sulfonimide lithium (LiTFSI) in a mixture of dioxolane (DOL) and 1,2-dimethoxyethane (DME) [1:1 v/v], ii) 1 M LiTFSI 0.05 M $LiNO_3$ in a mixture of DOL and DME (1:1 v/v). All the coin cells are made in dry atmospheric environment.

For asymmetric Cu|Li coin cells, modified/unmodified Cu (Pristine Cu and LTST-Cu) disks (1.6 cm diameter) and modified/unmodified Li (Pristine Li, $TiO_2$-Li, LTST-Li) are used as electrodes with the separator (Celgard 2500) and the electrolyte i (30 μl). The asymmetric coin cells are used to measure Coulombic efficiency of the systems. Current density and capacity of 1 mA $cm^{-2}$ and 1 mAh $cm^{-2}$ are used. For Li plating/stripping, galvanostatic condition is applied: 1 mA $cm^{-2}$ is applied for 1 h for plating and same current density is applied for stripping with a voltage cut off of 2 V; these procedures are repeated until desired number of cycles are achieved.

For symmetric Li coin cells, modified/unmodified Li (Pristine Li, $TiO_2$-Li, LTST-Li) disks (1.5 cm diameter) are used as the electrodes with the separator (Celgard 2500) and the electrolyte i (30 μl). The symmetric coin cells are cycled in galvanostatic condition with current density and capacity of 1 mA $cm^{-2}$ and 1 mAh $cm^{-2}$.

For Li-S cells, modified/unmodified Li (Pristine Li, $TiO_2$-Li, LTST-Li) disks, prepared sulfur cathode, separators (pristine or PEIrGO) and electrolytes i or ii are used. 30 μl of the electrolytes is injected to keep electrolyte/sulfur ratio under 10 μl $mg^{-1}$. Activation cycles are performed for 3 cycles at 0.1 C for the constant C rate performance cells.

### 2.4. Material characterizations

$TiO_2$ & LTST nanoparticles and rGO & PEIrGO are characterized by XPS analysis to investigate elemental and binding analysis. Thermogravimetric analysis is used to figure out sulfur content in the S/C composite for the sulfur cathode. Electrode morphologies and material coating thicknesses (See Fig. S4) are measured *via* scanning electron microscopy (SEM), and elemental mappings are done by energy dispersive X-ray spectroscopy (EDXS). For the AC impedance spectroscopy

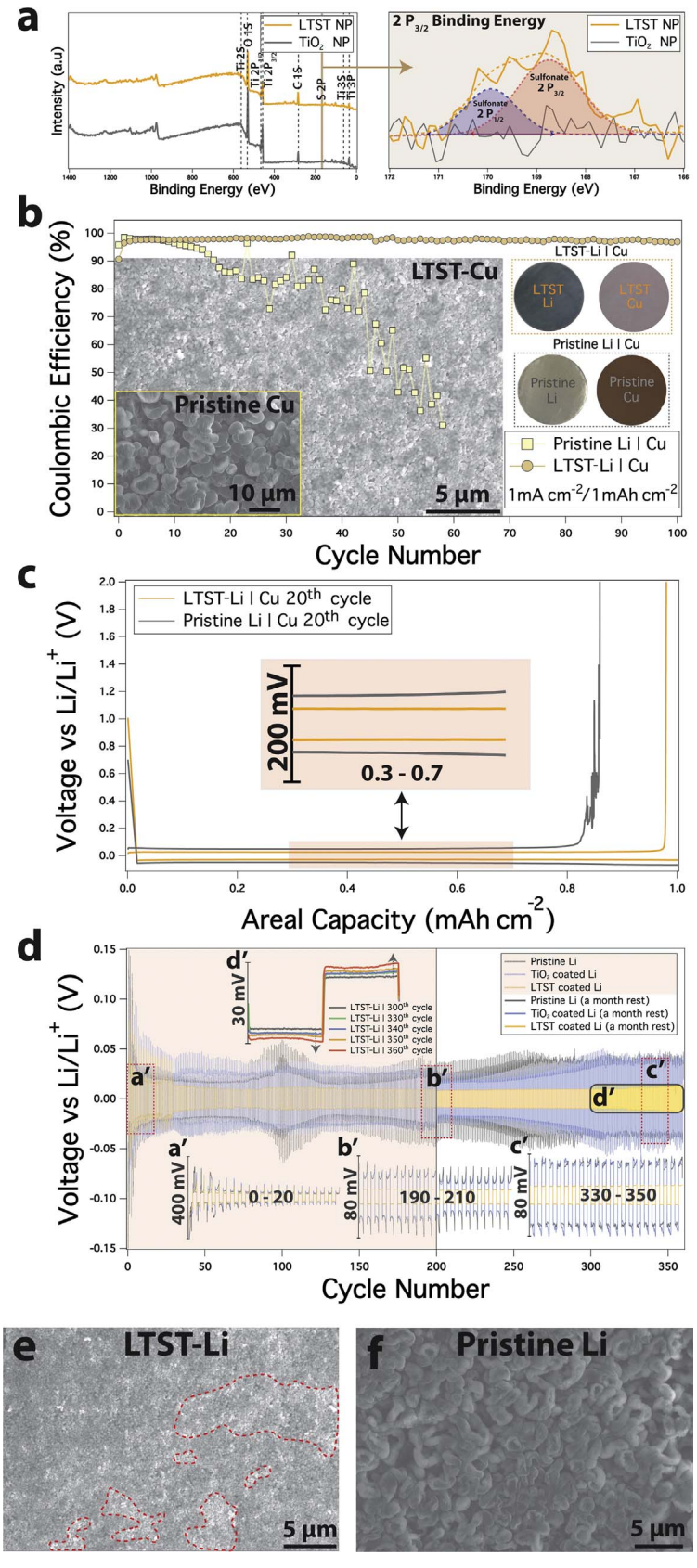


**Fig. 2.** Spectroscopic and electrochemical analysis of LTST-Li anode show that the ASEI on Li that is composed of functionalized nanoparticles improves electrochemical stability and cycling efficiency of the Li anode. **a)** Survey scan (left) and S 2P narrow scan (right) XPS spectra for $TiO_2$ and LTST nanoparticles. **b)** Coulombic efficiency as a function of cycle number for LTST-Li|Cu & Pristine Li|Cu asymmetric cells. The inset (inner left) SEM images show the surface of cycled LTST-Cu and pristine Cu. The inset (inner right) photos show fabricated LTST-Li & LTST-Cu and pristine Li & pristine Cu electrodes. **c)** Voltage profiles at the 20th cycle for LTST-Li|Cu and pristine Li|Cu asymmetric coin cells. **d)** Li plating/stripping voltage profiles for LTST-Li, $TiO_2$-Li, and pristine Li symmetric cells at a fixed current density of 1 mA $cm^{-2}$ and capacity of 1 mAh $cm^{-2}$. The insets are zoomed-in voltage profiles for the 0–20 cycles (a′), 190–210 cycles (b′), 330–350 cycles (c′), and 300–360 cycles (d′ – only LTST-Li). The transparent red region (up to 200th cycle) and colorless region (after 200th cycle) highlight the cell cycling performance before and after one-month rest period. **e)** Top view SEM image of cycled LTST-Li. **f)** Top view SEM image of cycled pristine Li. (For interpretation of the references to color in this figure legend, the reader is referred to the web version of this article.)

measurements, frequency range of 1 MHz to 0.5 Hz is used.

## 3. Results and discussion

### 3.1. Negatively-charged nanoparticle ASEI for lithium metal anode

X-ray photoelectron spectroscopy (XPS) was used to characterize the synthesized LTST nanoparticles. Fig. 2a shows survey (left) and narrow (right) S 2P XPS scans for $TiO_2$ and synthesized LTST nanoparticles. The survey spectra for LTST and $TiO_2$ show typical features for rutile $TiO_2$ nanoparticles,[53] including the Ti $2P_{3/2}$ (458.5 eV) and Ti $2P_{1/2}$ (464 eV) signals, O 1s signal (529.5 eV) and S 2P signals (168.5 eV and 169.8 eV) for LTST consistent with expectations for sulfonic acid attachment [54]. Qualitative support from this conclusion is readily obtained by comparing the ease with the pristine and functionalized $TiO_2$ nanoparticles in water, which shows that the functionalized particles are substantially more hydrophilic (Fig. S1). To verify physico-chemical stabilities of LTST with lithium, additional XPS measurement is performed on LTST-Li anode. The XPS result in Fig. S5 reveals that relatively small amount of $Li_2TiO_3$ exists as the XPS signal penetration depth is about 10 nm of exposed surfaces of the sample. To further verify electrochemical activity of LTST with lithium, cyclic voltammetry and galvanostatic cycling are performed for asymmetric configuration cells: i) Cu|Li, ii) $TiO_2$-Cu|Li, iii) LTST-Cu|Li (Fig. S6). Cyclic voltammograms show no visible and reversible redox reaction peaks that may correspond to reaction between the titania/LTST and lithium. Also, the galvanostatic voltage profiles of the samples show no reaction plateaus that match to the intercalation of lithium. Negligible current responses during anodic and cathodic sweeps and capacity from galvanostatic cyclings indicate that rutile titania and LTST are not seriously involving in electrochemical dynamics for the Li-S system.

To evaluate the effect of LTST on electrochemical interfaces, we characterized the Coulombic efficiency (CE) of lithium in Cu|Li asymmetric configuration coin cell in which the electrodes are coated with a thin layer of pristine or LTST nanoparticles. The measurements were performed at a fixed current density of 1 mA $cm^{-2}$ and capacity of 1 mAh $cm^{-2}$ (Fig. 2b). It is observed that the cell with 3 μm LTST coated on the Cu and Li electrodes exhibits high (~ 99%) CEs for more than 100 cycles. In contrast, the control cells exhibit severe CE decay after 20 cycles and the CE drops to < 50% after 50 cycles. These results provide evidence that a LTST particle coating on the electrodes improves the reversibility of the Li plating and stripping reactions at the Cu electrode. The inset in Fig. 2b (left) are SEM micrographs of LTST-Cu (large) and bare Cu (small) electrodes after 20 charge discharge cycles, while the inset (right) are photographs of the LTST coated Cu electrodes. It is noticed that whereas there is no evidence of uneven Li deposition on the LTST coated electrodes (Fig. S7), the deposition is rough and dendritic on the bare Cu electrode. It is further noted that at the deposition capacity of 1 mAh $cm^{-2}$ employed here, 4.8 μm of Li is moved during each cycle, which exceeds the thickness (3 μm) of the LTST ASEI. Assuming closely packed spherical particles, the Li volume moved each cycle is roughly ~ 47.7% of the LTST ASEI volume. Hence, roughly 30–31% of the total plating/stripping amount of Li is expected to fill the void space in the LTST ASEI. Thus, even without efforts to optimize the coating thickness and particle size, we see that these coatings are effective in both preventing dendritic deposition of Li and maintaining high CE.

The high and stable CE of LTST-Li apparent from our asymmetric cell studies can arise from at least three sources. First, it may result from the high interfacial conductivity (Fig. S8) at the electrode produced by the tethered film of lithium terminated polar $SO_3^-$ functionalized particle at the interface, which favors stable deposition of Li [55,56]. Second, because the deposited Li is hosted in the void network between interconnected particles, it may stabilize Li deposits against breakage and formation of disconnected/orphaned Li (Fig. S7), which lowers CE and cycliability of the electrodes. Finally, the negatively charged particle layer may restrict access of the anions and electrolyte solvent to the electrified electrode surface, which would increase electrochemical stability of the electrolyte. The potential profiles for the Cu|Li cells are reported in Fig. 2c. It is seen that the cells containing the LTST coated electrodes generally exhibit lower potential, and at that 20th cycle the plating and stripping potential values are 27.4 mV and 26.3 mV at 1 mA $cm^{-2}$. The corresponding values from cells that use the uncoated electrodes are noticeably higher, 54.6 mV and 56.5 mV at 1 mA $cm^{-2}$, and the noise at the end of the stripping process is due to Li ions having a disturbed migration under the thick/non-uniform and insulating SEIs, which potential fluctuates to keep the current constant. These results are consistent with the idea that the particle coating facilitates transport of ions at the electrolyte/electrode interfaces. This observation alone cannot determine, however, whether the source of the observation arises from ion transport facilitated by the charged groups on the LTST particles or from the coating's ability to limit anion/electrolyte degradation at the electrodes to form a thicker, more resistive SEI.

Electrochemical analysis of symmetric pristine Li, $TiO_2$-Li and LTST-Li cells were performed to investigate the effect of the nanoparticle coating on long-term cycling stability. Fig. 2d compares the voltage profiles for pristine Li, $TiO_2$-Li, and LTST-Li symmetric cells over 350 plate/strip cycles at 1 mA $cm^{-2}$ and capacity 1 mAh $cm^{-2}$. To analyze the potential evolution, inset figures are presented for 0–20th cycles (Fig. 2d, a′), 190–200th cycles (Fig. 2d, b′), 330–350th cycles (Fig. 2d, c′). Throughout the first 20 cycles, the LTST-Li exhibits the lowest overpotential, whereas pristine Li shows highly fluctuating dynamics indicative of unstable reformation of SEI and dendrites during successive cycles. The starting plating potential for symmetric cells based on pristine Li, $TiO_2$-Li, and LTST-Li electrodes are 23.52 mV, 24.82 mV, 16.66 mV, respectively, in agreement with findings from impedance spectroscopy analysis (Fig. S8), which show that the interfacial resistance of the electrodes decrease in the same sequence. It is also seen that the potential profiles for symmetric cells based on LTST-Li stabilizes after ~ 30 cycles where the potential spikes disappear, an indication that Li is reversibly and stably depositing and dissolving without undesired side reactions that promote potential hysteresis.

After 200 cycles, all the cells were rested for one month to evaluate the long-term physical and electrochemical stability of the ASEI coatings (Fig. 2d b′). After the rest period, all of the symmetric cells manifested reduced potential; however, the magnitude of the potential differences is different: LTST-Li (~ 6.1% reduction), $TiO_2$-Li (~ 13.8% reduction), and pristine Li (~ 16.1% reduction), indicating that the LTST coating is stable against long-term exposure to metallic Li and can at the same time provide long-term stability to the Li metal against parasitic reactions with electrolyte that would increase the thickness and resistance of the SEI. Moreover, stable cycling performance is achieved > 350 cycles for the LTST-Li symmetric cell whereas the $TiO_2$-Li and pristine Li show potential fluctuations and hysteresis (Fig. 2d, c′). Some voltage hysteresis is nonetheless observed for cells based on the LTST-Li between 300 and 360 cycles (Fig. 2d, d'). SEM images of LTST-Li (Fig. 2e) and pristine Li (Fig. 2f) electrodes taken after the 30th cycle shows no evidence of rough, dendritic deposition of Li and reveal uniform SEI (outside of the red regions indicated in Fig. 2e). High magnification SEM image of Fig. 2e (outside of red region) is shown in Fig. S9. We speculate that the potential flattening (after 30 cycles in Fig. 2d) starts when the uniform SEI covers the LTST. These results should be compared with those reported in Fig. 2f, which demonstrate rough Li deposition on the pristine Li electrode. Even though LTST ASEI effectively stabilized the Li transfer between the electrodes, increasing potential hysteresis after 350 cycles indicates that the LTST ASEI needs further improvement, such as optimization of the coating thickness, void fraction, and particle sizes. Efforts to address this issue are currently on the way.

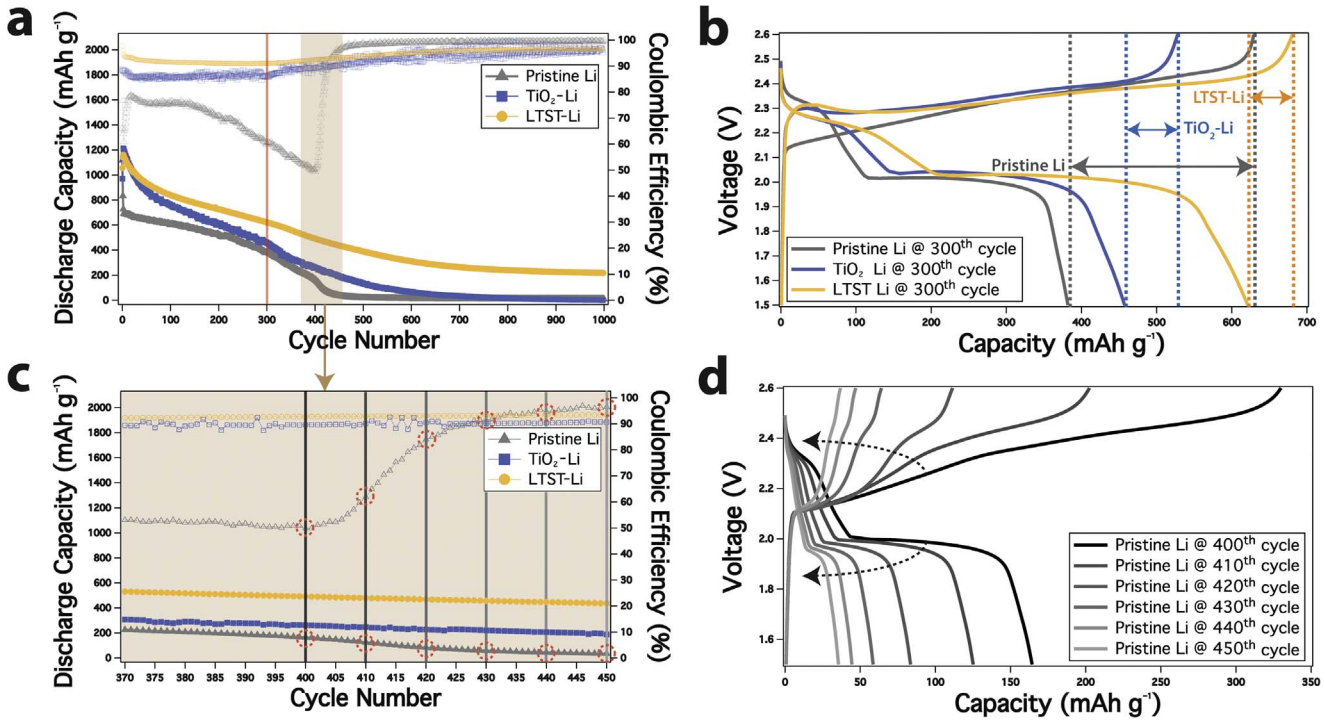


**Fig. 3.** Electrochemical analysis shows that the charged and morphology of the ASEI on Li influences performance of Li-S cell. **a)** Galvanostatic charge/discharge capacity (filled symbols) and Coulombic efficiency (open symbols) as a function of cycle number for LTST-Li|S, $TiO_2$-Li|S and pristine Li|S cells at a fixed rate of 0.5 C. None of the cells include $LiNO_3$ additives in the electrolyte. **b)** Voltage profiles at the 300th cycle (red vertical line in (a)) of the cells in (a). **c)** Discharge capacity (closed symbols) and Coulombic efficiency (open symbols) *versus* cycle number for cells in (a), focused on the 370–450 cycles. **d)** Voltage profiles for the pristine Li-S cell at the cycle numbers demarcated by vertical lines in (c). (For interpretation of the references to color in this figure legend, the reader is referred to the web version of this article.)

### 3.2. Effect of lithium metal protection on electrochemical performance of Li-S cells

Fig. 3 reports on the electrochemical performance of LTST-Li anode in half cells with the sulfur cathode. Cathodes with a fixed sulfur loading of 3 mg $cm^{-2}$, total cathode loading of 4.7 mg $cm^{-2}$, were used to observe in the study (Fig. 3a). Because our goal is to understand how the ASEI on the anode enhances interface stability, no $LiNO_3$ additive is used in the electrolyte, except where it is specifically noted. The LTST-Li anode is nonetheless seen to exhibit a high average CE of ~93%, compared to CE values of 87% and 68%, for cells based on $TiO_2$-Li and pristine Li electrodes, respectively. These results allow us to differentiate between the benefits provided by a simple passive nanoparticulate ASEI that limits electrolyte transport to the electrode and an active ASEI that can perform multiple additional functions. Although the $TiO_2$-Li showed moderate benefit for Li symmetric cell performance, the material is seen to clearly increase the CE in Li-S cells. This indicates that the intrinsic surface charge on the metal oxide particles and the nanoporous structure of the ASEI can to an extent limit parasitic reactions between the Li and soluble LiPS in the electrolyte. The noise in the CE may rise from the partial LiPS migration towards to the polar $TiO_2$ surface [57]. The LTST-Li, on the other hand, exhibits obvious and large improvements in CE and the results in the Fig. 3a show that these improvements can be retained to an extent for 1000 cycles. In comparison, Li-S cells based on pristine Li and $TiO_2$-Li electrodes reach their end of life in as little as 400 and 600 cycles, respectively. The improved CE of LTST-Li is further supported by comparing the voltage profiles of Li-S cells based on LTST-Li, $TiO_2$-Li and pristine Li anodes at the 300th cycle (Fig. 3b), as indicated as red line in Fig. 3a. A steep decrease of discharge capacity with increasing CE is observed, which usually indicates chemical shorting of Li-S cell when the electrode passivation leads to too high overpotentials to maintain stable cell operation.[34] Overall, two main factors can explain this phenomenon. i) nanoporous structure formed by the close packing of metal-oxide particles (LTST-Li & $TiO_2$-Li) acts as a mechanical barrier that reduces lithium/electrolyte contacts which eventually mitigate side reaction among lithium, electrolyte and LiPS, which increases CE in Li-S system. ii) The tethered Li and negatively charged/polar sulfonate groups work as ionic shields that favor Li migration and repel the polysulfides. The indication of the higher capacity retention for LTST-Li is due to improved preservation of active species that continue to get consumed *via* shuttling over repeated cycles.

The voltage profiles for the Li-S cells based on pristine Li electrode is displayed in Fig. 3d for 400–450 cycles. It is observed that while the capacity decreases rapidly the overpotential changes are modest, and the CE actually rises. These features are consistent with cell failure due to depletion of active material in one or both electrodes. The source is clearer if one compares the CE profiles for the Li-S cells based on pristine Li and LTST-Li anodes. For such cells, large improvements in CE are seen, but there are only modest gains in terms of capacity retention. These results lead us to conclude that the retention of sulfur in the cathode and reutilization of the active material is the source of the capacity failure in both cases.[38] Therefore, complementary efforts to those used to stabilize the anode are needed to stabilize the sulfur cathode for stable, long-term Li-S cell operation.

### 3.3. Positively-charged nanoparticle ASEI for the sulfur cathode

There are a number of approaches reported in the literature for synthesizing advanced sulfur hosts that restrict LiPS dissolution and improve sulfur reutilization in the Li-S battery cathode. Here, we build on our previous efforts that focus on modifying the cathode facing side of the separator with an ASEI able to limit active material loss and to improve sulfur utilization in the cathode [8,9]. This approach is preferred because it can be straightforwardly implemented on conventional separators (*i.e.* Celgard), enabling direct comparisons with results in the previous sections to elucidate and remedy the underlying causes of capacity fade. We employ PEIrGO as an ASEI on the cathode facing

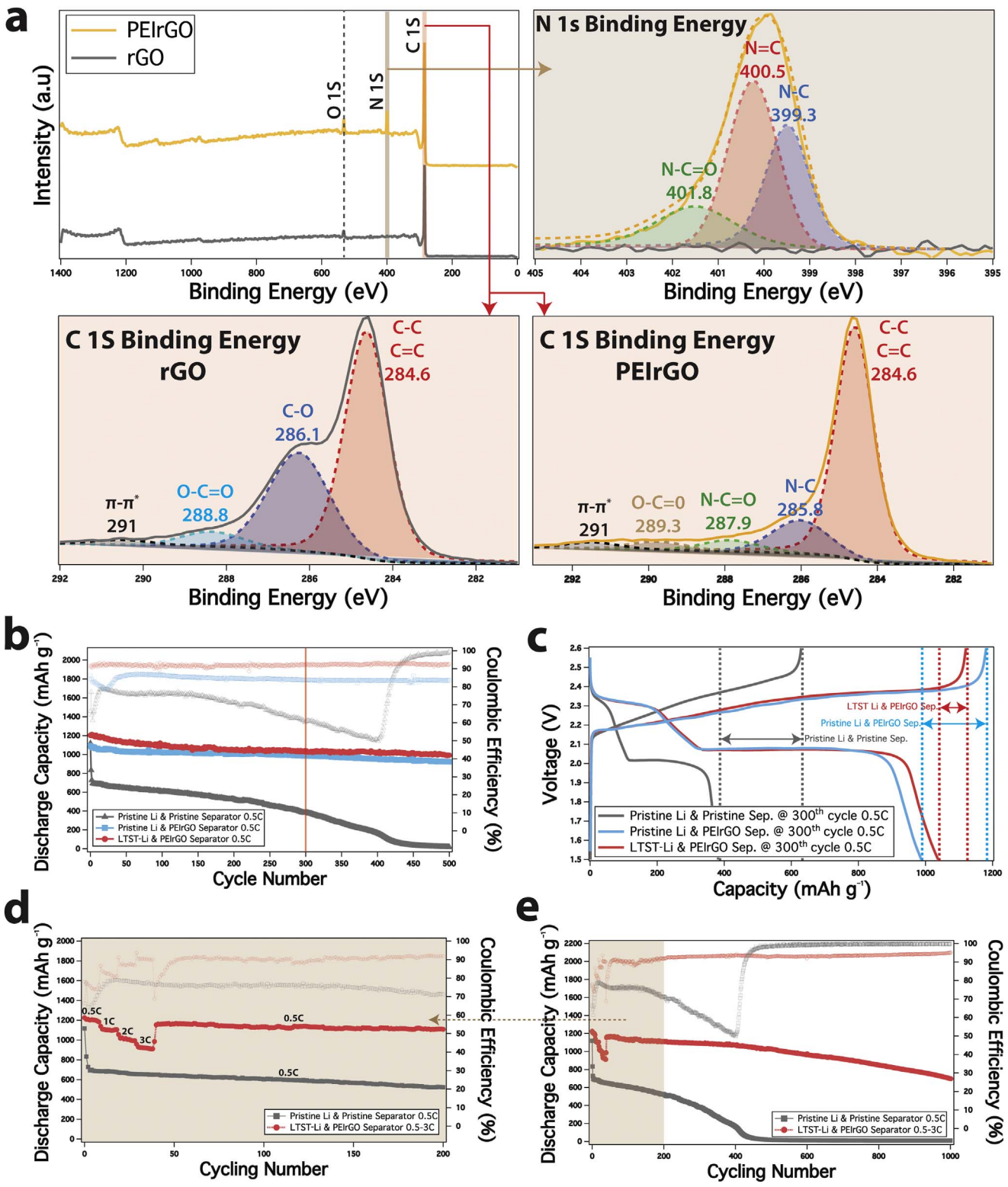


**Fig. 4.** The sulfur cathode in Li-S cells is stabilized by an ASEI based on PEIrGO. **a)** Survey scan XPS spectrum (upper left), N 1s narrow scan (upper right), C 1s narrow scan (bottom left and right) for rGO and PEIrGO. **b)** Galvanostatic charge/discharge capacity (filled symbols) and Coulombic efficiency (open symbols) for LTST-Li|PEIrGO|S, pristine Li|PEIrGO|S and pristine Li|S cells at 0.5 C. These cells do not contain $LiNO_3$ additives in the electrolyte. **c)** Voltage profiles at the 300th cycle (red vertical line in (b)) for each of the Li-S cell configurations in (b). **d)** Galvanostatic charge/discharge performance at various C rates (0.5–3 C) for LTST-Li|PEIrGO|S and pristine Li|S cells. **e)** Extended cycling performance of cells in (d). (For interpretation of the references to color in this figure legend, the reader is referred to the web version of this article.)

side of the separator for its dual ability to bind LiPS using amine groups on the PEI polymer, [8,58] and to facilitate electrochemical access to and reutilization of intercepted LiPS by means of the high electronic conductivity of the rGO framework. Fig. 4a shows XPS spectra of PEIrGO and rGO and verifies the attachment of PEI on rGO. The most apparent differences are observed from the N 1s and C 1s peaks that amine (399.3 eV) and amide (401.8 eV) as well as N-C (285.8 eV) and N-C=O (287.9 eV) peaks [58].

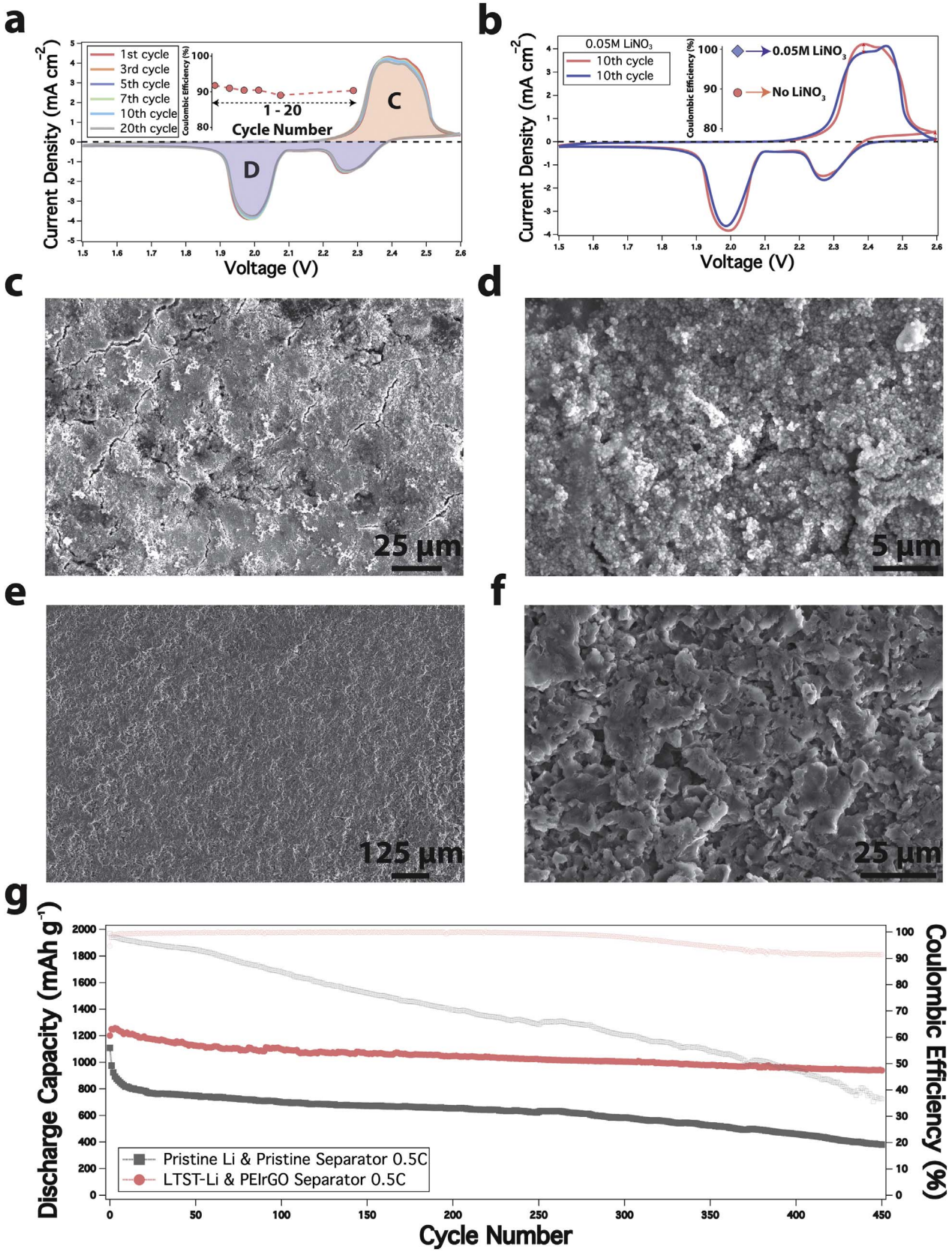


**Fig. 5.** Characterizing the stabilizing effects of LTST and PEIrGO on Li-S electrodes. **a)** Cyclic voltammograms of LTST-Li|PEIrGO|S cell at a scan rate of 0.1 mV $s^{-1}$. The inset shows the calculated Coulombic efficiency up to the 20th cycle. **b)** Same as (a), but for the 10th cycle; the blue markers show the effect of 0.05 M $LiNO_3$ as an electrolyte additive. **c)** Top view SEM image of cycled LTST-Li anode. **d)** Same as (c), but at higher magnification. **e)** Top view SEM image of cycled PEIrGO. **f)** Same as (e), but at higher magnification. **g)** Galvanostatic charge/discharge capacity (closed symbols) and Coulombic efficiency (open symbols) for LTST-Li|PEIrGO|S and pristine Li|S cells at a fixed rate of 0.5 C with 0.05 M $LiNO_3$ as electrolyte additive. (For interpretation of the references to color in this figure legend, the reader is referred to the web version of this article.)

To create an ASEI on the separator, the synthesized PEIrGO is first mixed with pure ethanol to form a low-viscosity ink that can be air sprayed onto the separator to produce a uniform 10 μm PEIrGO coating. Fig. 4b compares cycling performance of pristine electrodes, Li|-PEIrGO|S and LTST-Li|PEIrGO|S cells; the same cathode active mass loading reported in the previous section is employed. The results show that the PEIrGO itself provides improved capacity retention (80% over 500 cycles) with improved CE (84%) compared with that of pristine separator case (15% over 400 cycles with 68% CE). The LTST-Li|-PEIrGO|S cells exhibit improved CE of approximately 92% with capacity retention of 83% over 500 cycles. As expected, anode protection indeed helps CE whereas the long-term cycling performance is a stronger function of separator modification due to enhanced interception and reutilization of dissolved LiPS. It is understood, however, that the two effects are coupled and that in a practical Li-S cell with a minimal excess of Li, both types of ASEIs will be required for long cycle life.

The above conclusions are supported by more careful assessment of the voltage profiles in Fig. 4c. The PEIrGO separators show decreased overpotential with curtailed overcharge for LTST-Li & Li|PEIrGO|S cells. To evaluate the rate performance of the LTST-Li|PEIrGO|S cells electrochemical cycling measurements were performed at rates between 0.5 C and 3 C (Fig. 4d). About 25% capacity fluctuation is observed from 0.5C to 3 C and ~50% of the initial capacity is retained up to 1000 cycles.

Further support for the effects of the LTST ASEI electrostatic shielding layer for Li and PEIrGO coatings on the separator was obtained using cyclic voltammetry and SEM analysis (Fig. 5). Fig. 5a shows results from cyclic voltammetry measurements at a scan rate of 0.1 mV $s^{-1}$ for 20 cycles of the Li-S cell operation. The current polarity tells the direction of the current flow, and therefore the amount of current collected during cathodic and anodic sweeps indicates the total charges flew during each sweep direction. Hence, by taking the average current ratio between the anodic (discharge) and cathodic (charge) currents, it is possible to estimate the CE of the cells from the measurements. The calculated CE is shown in the inset of Fig. 5a to be around 91%, in agreement with the CE obtained from the galvanostatic cycling results in Fig. 5b. Fig. 5b compares the CV of the modified Li-S cell with/without 0.05 M $LiNO_3$ additive in the electrolyte. It is seen that even at such low concentration the additive has a large, positive effect, with CE values quickly reaching > 99%. Figs. 5c and d shows enlarged and zoomed-in SEM micrographs of cycled LTST-Li (Fig. 4e). It is apparent that Li dendrites formations are effectively suppressed. To evaluate the mechanical stability of the PEIrGO layer, cycled PEIrGO-coated separators were also interrogated *via* SEM (Figs. 5e and f) and the PEIrGO layer is seen to be well preserved. Elemental mappings of the PEIrGO layer are shown in Fig. S10, which support our hypothesis that LiPS is trapped by the PEIrGO SEI. Fig. 5g shows the effect of $LiNO_3$ additive in the electrolyte on cycling performance. It is seen that LTST-Li|PEIrGO|S cells with as little as 0.05 M $LiNO_3$ exhibit stable electrochemical performance, with CE > 99%; however, the $LiNO_3$ is evidently consumed by the 300 cycles and CE reverts to values (~ 92%) found in the base electrolyte. This loss of $LiNO_3$ is expected because the additive known to decomposes below 1.7 V, [46] which is above the cut-off voltage (1.5 V) employed in the study.

## 4. Conclusion

In conclusion, we have demonstrated that ionically shielding nanomaterial composites can be used to create artificial solid electrolyte interphases for the anode and cathode of Li-S system. We show that protecting the lithium anode *via* a nanoporous ASEI on Li composed of negatively-charged metal-oxide nanoparticle film stabilizes Li surfaces by physical and chemical means and results in large increases (from 65% to > 90%) in Coulombic efficiency of Li-S cells in electrolytes that do not contain $LiNO_3$ as additive. It is also shown that a positively-charged interphase/buffer layer composed of a PEIrGO ASEI on the cathode-facing surface of the separator facilitates exceptionally high sulfur reutilization by interception of dissolved LiPS and by facilitated electron transport. When these two approaches are paired, robust rechargeable Li-S systems are achieved that exhibit > 80% capacity retention over 500 cycles and > 90% Coulombic efficiency.

## Acknowledgements

This work was supported by the National Research Foundation of Korea (NRF-2016M1B3A1A01937324), and the Korea Institute of Science and Technology (KIST) Institutional Program (Project no. 2E27061)

## Appendix A. Supporting information

Supplementary data associated with this article can be found in the online version at http://dx.doi.org/10.1016/j.nanoen.2017.10.018.

## References

[1] D. Aurbach, E. Zinigrad, Y. Cohen, H. Teller, Solid State Ion. 148 (2002) 405–416.
[2] Y. Lu, Z. Tu, L.A. Archer, Nat. Mater. 13 (2014) 961–969.
[3] M.D. Tikekar, S. Choudhury, Z. Tu, L.A. Archer, Nat. Energy 1 (2016) 1–7.
[4] Z. Tu, M.J. Zachman, S. Choudhury, S. Wei, L. Ma, Y. Yang, L.F. Kourkoutis, L.A. Archer, Adv. Energy Mater. (2017) 1602367.
[5] X. Ji, K.T. Lee, L.F. Nazar, Nat. Mater. 8 (2009) 500–506.
[6] N. Jayaprakash, J. Shen, S.S. Moganty, A. Corona, L.A. Archer, Angew. Chem. 50 (2011) 5904–5908.
[7] H. Wang, Y. Yang, Y. Liang, J.T. Robinson, Y. Li, A. Jackson, Y. Cui, H. Dai, Nano Lett. 11 (2011) 2644–2647.
[8] M.S. Kim, L. Ma, S. Choudhury, L.A. Archer, Adv. Mater. Interfaces 3 (2016) 1600450.
[9] M.S. Kim, S. Choudhury, S.S. Moganty, S. Wei, L.A. Archer, J. Mater. Chem. A 4 (2016) 14709–14719.
[10] G. Girishkumar, B. Mccloskey, A.C. Luntz, S. Swanson, W. Wilcke, Phys. Chem. Lett. 1 (2010) 2193–2203.
[11] H. Jung, J. Hassoun, J. Park, Y. Sun, B. Scrosati, Nat. Chem. 4 (2012) 579–585.
[12] S. Lau, L.A. Archer, Nano Lett. 15 (2015) 5995–6002.
[13] M.D. Slater, D. Kim, E. Lee, C.S. Johnson, Adv. Funct. Mater. 23 (2013) 947–958.
[14] M.S. Islam, C.A.J. Fisher, Chem. Soc. Rev. 43 (2014) 185–204.
[15] S. Wei, S. Choudhury, J. Xu, P. Nath, Z. Tu, L.A. Archer, Adv. Mater. 29 (2017) 1605512.
[16] B. Dunn, H. Kamath, J. Tarascon, Science 334 (2011) 1212741.
[17] S. Wei, S. Xu, A. Agrawral, S. Choudhury, Y. Lu, Z. Tu, L. Ma, L.A. Archer, Nat. Commun. 7 (2016) 1–10.
[18] P. Hartmann, C.L. Bender, M. Vrať, A.K. Dürr, A. Garsuch, J. Janek, P. Adelhelm, Nat. Mater. 12 (2013) 228–232.
[19] S.K. Das, S. Lau, L.A. Archer, J. Mater. Chem. A 2 (2014) 12623–12629.
[20] Q. Li, N.J. Bjerrum, J. Power Sources 110 (2002) 1–10.
[21] M. Lin, M. Gong, B. Lu, Y. Wu, D. Wang, M. Guan, M. Angell, C. Chen, J. Yang, B.-J. Hwang, H. Dai, Nature 520 (2015) 324–328.
[22] S. Licht, D. Peramunage, J. Electrochem. Soc. 140 (1993) 19–21.
[23] G. Cohn, L. Ma, L.A. Archer, J. Power Sources 283 (2015) 416–422.
[24] D.D. Macdonald, S. Real, S.I. Smedley, M. Urquidi-macdonald, S.R.I. International, M. Park, J. Electrochem. Soc. 135 (1988) 2410–2414.
[25] S. Yang, H. Knickle, J. Power Sources 112 (2002) 162–173.
[26] W.I. Al Sadat, L.A. Archer, Sci. Adv. 2 (2016) e1600968.
[27] M. Armand, J.-M. Tarascon, Nature 451 (2008) 652–657.
[28] P.G. Bruce, S.A. Freunberger, L.J. Hardwick, J.-M. Tarascon, Nat. Mater. 11 (2011) (172–172).
[29] D. Larcher, J.-M. Tarascon, Nat. Chem. 7 (2015) 19–29.
[30] Y.V. Mikhaylik, J.R. Akridge, J. Electrochem. Soc. 151 (2004) A1969–A1976.
[31] S.-E. Cheon, K.-S. Ko, J.-H. Cho, S.-W. Kim, E.-Y. Chin, H.-T. Kim, J. Electrochem. Soc. 150 (2003) A800.
[32] X. Chen, T. Hou, B. Li, C. Yan, L. Zhu, C. Guan, Energy Storage Mater (2017), http://dx.doi.org/10.1016/j.ensm.2017.01.003.
[33] R. Cao, W. Xu, D. Lv, J. Xiao, J. Zhang, Adv. Energy Mater. 5 (2015) 1402273.
[34] L. Qie, C. Zu, A. Manthiram, Adv. Energy Mater. 6 (2016) 1502459.
[35] R. Cao, J. Chen, K.S. Han, W. Xu, D. Mei, P. Bhattacharya, M.H. Engelhard, K.T. Mueller, J. Liu, J.G. Zhang, Adv. Funct. Mater. 26 (2016) 3059–3066.
[36] H.J. Peng, W.T. Xu, L. Zhu, D.W. Wang, J.Q. Huang, X.B. Cheng, Z. Yuan, F. Wei, Q. Zhang, Adv. Funct. Mater. 26 (2016) 6351–6358.
[37] C. Yan, X. Cheng, C. Zhao, J. Huang, S. Yang, J. Power Sources 327 (2016) 212–220.
[38] A.C. Kozen, C.-F. Lin, A.J. Pearse, M.A. Schroeder, X. Han, L. Hu, S.B. Lee, G.W. Rubloff, M. Noked, ACS Nano 9 (2015) 5884–5892.
[39] W. Li, H. Yao, K. Yan, G. Zheng, Z. Liang, Y. Chiang, Y. Cui, Nat. Commun. 6 (2015) 7436.

[40] J.S. Kim, D.W. Kim, H.T. Jung, J.W. Choi, Chem. Mater. 27 (2015) 2780–2787.
[41] Y. Z, J.-G.Z. Wu Xu, Jiulin Wang, Fei Ding, Xilin Chen, Eduard Nasybulin, Energy Environ. Sci. 7 (2014) 513–537.
[42] X. Cheng, H. Peng, J. Huang, R. Zhang, C. Zhao, Q. Zhang, ACS Nano 9 (2015) 6373–6382.
[43] M.D. Tikekar, L.A. Archer, D.L. Koch, Sci. Adv. 2 (2016) 1600320.
[44] J. Qian, B.D. Adams, J. Zheng, W. Xu, W.A. Henderson, J. Wang, M.E. Bowden, S. Xu, J. Hu, J.G. Zhang, Adv. Funct. Mater. 26 (2016) 7094–7102.
[45] J. Qian, W.A. Henderson, W. Xu, P. Bhattacharya, M. Engelhard, O. Borodin, J.-G. Zhang, Nat. Commun. 6 (2015) 6362.
[46] R. Fang, S. Zhao, Z. Sun, D.-W. Wang, H.-M. Cheng, F. Li, Adv. Mater. (2017) 1606823.
[47] T. Tao, S. Lu, Y. Fan, W. Lei, S. Huang, Y. Chen, Adv. Mater. 1700542 (2017) 1–19.
[48] G. Ma, Z. Wen, M. Wu, C. Shen, Q. Wang, J. Jin, X. Wu, Chem. Commun. 50 (2014) 14209–14212.
[49] C. Huang, J. Xiao, Y. Shao, J. Zheng, W.D. Bennett, D. Lu, S.V. Laxmikant, M. Engelhard, L. Ji, J. Zhang, X. Li, G.L. Graff, J. Liu, Nat. Commun. 5 (2014) 1–7.
[50] J.-Q. Huang, Q. Zhang, H.-J. Peng, X.-Y. Liu, W.-Z. Qian, F. Wei, Energy Environ. Sci. 7 (2014) 347.
[51] N.I. Kovtyukhova, P.J. Ollivier, B.R. Martin, T.E. Mallouk, S.A. Chizhik, E.V. Buzaneva, A.D. Gorchinskiy, Chem. Mater. 11 (1999) 771–778.
[52] W.S. Hummers, R.E. Offeman, J. Am. Chem. Soc. 80 (1958) (1339–1339).
[53] L. Li, J. Yan, T. Wang, Z.-J. Zhao, J. Zhang, J. Gong, N. Guan, Nat. Commun. 6 (2015) 5881.
[54] M.M. Nasef, H. Saidi, H.M. Nor, M.A. Yarmo, J. Appl. Polym. Sci. 76 (2000) 336–349.
[55] X.B. Cheng, T.Z. Hou, R. Zhang, H.J. Peng, C.Z. Zhao, J.Q. Huang, Q. Zhang, Adv. Mater. 28 (2016) 2888–2895.
[56] Z. Liang, G. Zheng, C. Liu, N. Liu, W. Li, K. Yan, H. Yao, P.C. Hsu, S. Chu, Y. Cui, Nano Lett. 15 (2015) 2910–2916.
[57] X. Liu, J.-Q. Huang, Q. Zhang, L. Mai, Adv. Mater. (2017) 1601759.
[58] L. Ma, H.L. Zhuang, S. Wei, K.E. Hendrickson, M.S. Kim, G. Cohn, R.G. Hennig, L.A. Archer, ACS Nano 10 (2016) 1050–1059.

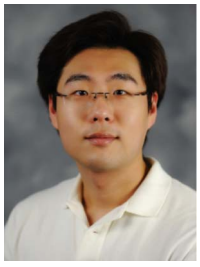

**Mun Sek Kim** received B.S. degree in Chemical Engineering from University California, Berkeley in 2014 and M.S. degree in Chemical & Biomolecular Engineering from Cornell University in 2016. He is now a professional research scientist at Korea Institute of Science and Technology in Energy Convergence Research Center. His research is mainly focused on the lithium metal secondary battery systems.

**Min-Seop Kim** received his B.S. (2012) and M.S. (2014) degrees in Department of Materials Science and Engineering from University of Seoul. Now, he is the Ph.D. candidate in Department of Materials Science and Engineering at Korea University and collaborates on a work with Korea Institute of Science and Technology. His main research area is developing lithium-sulfur batteries.

**Vandung Do** received B.S degree in Engineering Physics from Vietnam National University, Hanoi in 2009, and M.S. in Electrical and Computer Engineering from Ajou University in 2014. He is now a Ph.D. candidate at Department of Energy and Environment Technology, Korea University of Science and Technology. His research is mainly focused on cathode materials for lithium sulfur batteries.

**Young Rok Lim** received Ph.D. in Department of Chemistry from Korea University in 2017. He is actively involved in Li-ion battery researches at Korean Institute of Science and Technology in Energy Convergence Research Center. He is now a research professor at Korea University. His research is mainly focused on the lithium secondary batteries.

**In Wook Nah** is currently a senior researcher at Korea Institute of Science and Technology in Energy Convergence Research Center. He received his Ph.D. in chemical engineering from Yonsei University in 2009. His research is mainly focused on the nanostructured materials for $CO_2$ capture/conversion, liquefaction of hydrogen storage, and secondary batteries.

**Lynden A. Archer** is the James A. Friend Family Distinguished Professor of Chemical and Biomolecular Engineering at Cornell University. He received his B.S. degree in chemical engineering from the University of Southern California in 1989 and a Ph.D. in chemical engineering from Stanford University in 1993. He was a postdoctoral member of the technical staff at AT & T Bell Laboratories. He is a fellow of the American Physical Society. His research focuses on transport properties of polymers and organic-inorganic hybrid materials, and their applications for electrochemical energy storage.

**Won Il Cho** is a principal researcher at Korea Institute of Science and Technology in Energy Convergence Research Center. He received his Ph.D. in metallurgy from Korea University in 1992. He was a postdoctoral fellow of materials science department at Northwestern University. He was a head of next generation battery research center at Korea Electronics Technology Institute and advanced battery research center at KIST. He is Vice President of Korean Electrochemical Society and will be President starting next year. His research mainly deals with materials for novel battery systems and electrode materials, thin film fabrication and analysis.